The Astrophysical Journal, 582:82–94, 2003 January 1

TRACING THE WARM-HOT INTERGALACTIC MEDIUM AT LOW REDSHIFT: X-RAY FOREST OBSERVATIONS TOWARD H1821+643

Smita Mathur,[1] David H. Weinberg,[1] and Xuelei Chen[2,3]

Received 2002 June 5; accepted 2002 August 29

ABSTRACT

We present a high-resolution ($\lambda/\Delta\lambda \approx 500$) X-ray spectrum of the bright quasar H1821+643 ($z = 0.297$), obtained in a 470 ks observation with the *Chandra X-Ray Observatory*. We search for X-ray absorption by highly ionized metal species, O VII and O VIII in particular, at the redshifts of the six intervening O VI absorption systems known from UV studies. We detect features with $\gtrsim 2\,\sigma$ significance at the predicted O VII and O VIII wavelengths of one O VI system, at the O VII wavelength of a second, and at the Ne IX wavelength of a third. We find two additional features of comparable strength (one O VII and one O VIII) within 1000 km s^{-1} of the O VI redshifts. The 1 σ constraints on the relative abundances of different species imply significant variations from system to system in f(O VI), the fraction of oxygen in the O VI state. The constraints in the two detected O VI systems imply gas overdensities lower than the values $\delta \gtrsim 100$ expected in virialized systems, suggesting that the absorption arises in lower density, filamentary structures. At the 2 σ level, however, the physical constraints are weak, although all of the systems must have temperature $T < 10^6$ K to be consistent with upper limits on O VII. If we treat our 2 σ detections of known O VI systems as real, but assume minimal O VII and O VIII in the other systems, we estimate $[f(\mathrm{O\,VI}) + f(\mathrm{O\,VII}) + f(\mathrm{O\,VIII})]/f(\mathrm{O\,VI}) = 32 \pm 9$ for the average ratio of all highly ionized oxygen species to O VI. Combined with estimates of the total column density of O VI absorption per unit redshift, this ratio implies that the total baryon fraction associated with detected O VI absorbers is $\Omega_b(\mathrm{O\,VI}) \sim 0.03\ h_{70}^{-1}$, a substantial fraction of the baryon density predicted by big bang nucleosynthesis and larger than that associated with stars or with gas detected in 21 cm or X-ray emission. Because of the limited signal-to-noise ratio of the detections, these results must be treated with caution. Nonetheless, the combination of the O VI data with these X-ray forest measurements provides the most direct evidence to date for the pervasive, moderate-density, shock-heated intergalactic medium predicted by leading cosmological scenarios. The high inferred incidence of relatively strong O VII and O VIII absorption implies that some regions of the intergalactic medium are enriched to a level substantially above [O/H] = −1.

Subject headings: cosmology: observations — galaxies: active — intergalactic medium — quasars: absorption lines — quasars: individual (H1821+643) — X-rays: galaxies

1. INTRODUCTION

Much of our knowledge of the intergalactic medium (IGM) comes from the rest-frame UV line absorption that it imprints on the spectra of background quasars: the Lyα forest of neutral hydrogen and associated metal lines such as C IV and O VI. The Lyα forest is produced mainly by diffuse, photoionized gas at temperatures $T \sim 10^4$ K, and it appears to trace the main reservoir of cosmic baryons at high redshift (Rauch & Haehnelt 1995; Hernquist et al. 1996; Rauch et al. 1997; Weinberg et al. 1997). The Lyα forest thins out at low redshift, and cosmological simulations predict that the continuing process of structure formation heats a substantial fraction of intergalactic gas to temperatures at which it produces little hydrogen Lyα absorption, and at which the dominant ionization stages of heavier elements have absorption transitions at X-ray wavelengths rather than UV. Hot, dense gas in the central regions of galaxy clusters and groups can be detected by its X-ray emission, but most of the shock-heated gas resides in the outskirts of virialized halos and in lower density filamentary structures, making its continuum emission weak. One of the few prospects for detecting this low-density shock-heated gas is via the "X-ray forest" of absorption lines it should produce in quasar spectra (Hellsten, Gnedin, & Miralda-Escudé 1998; Perna & Loeb 1998; Fang & Canizares 2000; Chen et al. 2002; Fang, Bryan, & Canizares 2002a). Nicastro et al. (2002) find strong evidence for absorption by highly ionized oxygen and neon at $z \approx 0$, but there have been no clear detections to date of intergalactic X-ray absorption originating beyond the Local Group. This paper describes a search for X-ray forest absorption toward H1821+643 ($z = 0.297$) using a high-resolution ($\lambda/\Delta\lambda \approx 500$) spectrum obtained in a 470 ks observation with the *Chandra X-Ray Observatory*.

The baryon density implied by big bang nucleosynthesis (BBN) and the estimated primordial deuterium abundance, $\Omega_{\mathrm{BBN}} \approx 0.04\ h_{70}^{-2}$ (Burles & Tytler 1997, 1998; here $h_{70} \equiv H_0/70$ km s^{-1} Mpc^{-1}), exceeds the density of baryons in known stars and X-ray–emitting gas by roughly an order of magnitude (Fukugita, Hogan, & Peebles 1998). The lower density regime of the "warm-hot intergalactic medium" (WHIM; a term coined by Cen & Ostriker [1999a] to refer to gas in the temperature range 10^5–10^7 K) could constitute a major fraction of the "missing" low-redshift baryons. Hydrodynamic cosmological simulations predict

[1] Astronomy Department, 140 West 18th Avenue, Ohio State University, Columbus, OH 43210; smita@astronomy.ohio-state.edu, dhw@astronomy.ohio-state.edu.

[2] Physics Department, 174 West 18th Avenue, Ohio State University, Columbus, OH 43210.

[3] Institute for Theoretical Physics, University of California, Santa Barbara, CA 93106; xuelei@itp.ucsb.edu.

that 30%–50% of the baryons reside in this phase at $z = 0$ (Cen & Ostriker 1999a; Davé et al. 1999, 2001). *Hubble Space Telescope* (*HST*) and *Far Ultraviolet Spectroscopic Explorer* (*FUSE*) detections of O VI $\lambda\lambda$1032, 1038 absorption lines toward H1821+643 and PG 0953+415 (Tripp, Savage, & Jenkins 2000, hereafter TSJ; Tripp & Savage 2000; Oegerle et al. 2000; Savage et al. 2002) offer a tantalizing hint of this baryon reservoir. Adopting conservative assumptions of $[O/H] = -1$ and an O VI ionization fraction $f(O\,VI) = 0.2$ (which is close to the maximum in photoionization or collisional ionization), TSJ conclude that the gas associated with these weak O VI absorbers accounts for $\Omega_b \approx 0.004\, h_{70}^{-1}$ of the cosmic baryon budget, comparable in total mass to all other known low-redshift components combined. They remark, moreover, that $f(O\,VI)$ could plausibly be much lower than 0.2, implying a substantially higher baryon fraction. For most reasonable assumptions about the physical conditions of this absorbing gas, the dominant ionization state should be O VII or O VIII. Gas hotter than $T \sim 5 \times 10^5$ K would have very low $f(O\,VI)$, so it might produce O VII or O VIII absorption with no detectable O VI.

We chose H1821+643 for our X-ray forest search in part because it is one of the brightest X-ray quasars at moderate redshift, and in part because it has been studied carefully for intervening O VI absorption (TSJ; Oegerle et al. 2000). Theoretical expectations for X-ray forest absorption depend strongly on the assumed metallicity distribution of the moderate-density shock-heated IGM, a subject on which there is little empirical guidance. However, for metallicities $Z \sim 0.1$–$0.3\ Z_\odot$, simulations and analytic calculations predict few O VII or O VIII lines above column density $N \sim 2 \times 10^{15}$ cm^{-2} (Hellsten et al. 1998; Perna & Loeb 1998; Fang & Canizares 2000; Chen et al. 2002; Fang et al. 2002a) and weaker absorption by other elements, so even long exposures with *Chandra* or *XMM-Newton* are unlikely to detect absorption at a high signal-to-noise ratio (S/N). Searching at redshifts with known O VI absorption allows one to adopt a lower effective threshold for significant detection, greatly increasing the odds of success. Furthermore, detections of or upper limits on X-ray absorption provide new constraints on the physical conditions of the O VI absorbers.

We chose the duration of our spectroscopic observation so that if $[f(O\,VI) + f(O\,VII) + f(O\,VIII)]/f(O\,VI) \sim 30$, a physically plausible ratio that would imply that O VI absorbers contain a large fraction of the "missing" low-redshift baryons, then we would clearly detect the strongest of the TSJ systems, and we would detect the next two strongest systems at the 2–3 σ level. As we show below, we find only a $\sim$1 σ signal from the strongest TSJ system, but we obtain $\approx$2 σ detections of O VII from the next strongest system and of O VII and O VIII from the O VI system discovered by Oegerle et al. (2000). We also find features that could correspond to oxygen absorption at other redshifts close to the detected systems (within 1000 km s^{-1}) and a possible signature of Ne IX absorption from one system. The best estimate of the mean $[f(O\,VI) + f(O\,VII) + f(O\,VIII)]/f(O\,VI)$ from our data is $\sim$30, but the moderate statistical significance of our detections and the implied variation in $f(O\,VI)$ from system to system leave the interpretation of our results more ambiguous than we would like. Nonetheless, this observation provides the strongest evidence to date for the moderate-density shock-heated IGM predicted by theoretical models, and the detections and upper limits have important implications for the physical state of the O VI absorption systems and for their connection to the missing baryons of the low-redshift universe. We proceed to a description of the observations, data reduction, and absorption-line analysis, then to a discussion of these implications.

2. OBSERVATIONS AND DATA REDUCTION

We observed H1821+643 with *Chandra* between 2001 January 17 and January 24, for a total exposure time of 470 ks. The observation was divided into four different parts: observation IDs 2186, 2418, 2310, and 2311. We used the low-energy transmission grating (LETG; Brinkman et al. 1997) with the advanced CCD imaging camera for spectroscopy (ACIS-S; C. R. Canizares et al. 2003, in preparation). Our primary interest is in O VII and O VIII lines with rest wavelengths of 21.602 and 18.969 Å, respectively, and thus in the observed wavelength range of 18.9–28 Å that runs from O VIII at $z = 0$ to O VII at the quasar redshift $z = 0.297$. Since the lines are expected to be low S/N, it is important to optimize the instrument response in this interval. To avoid the S3/S4 chip gap between 21.2 and 21.8 Å, the aim point was offset by 2′ in the $+Y$-direction. This offset moves the chip gap to 27.9–28.5 Å, so the entire first-order spectrum in the wavelengths of interest is now on S3. Since the telescope focus is on S3, this choice enhances the effective area around 25 Å. To ameliorate the effects of charge transfer inefficiency for spectral order sorting, a scientific instrument module Z-direction offset of -8 mm was chosen. Accordingly, an ACIS-S subarray with rows 49–256 was used.

The shift of the aim point, essential for optimizing wavelength coverage and effective area in the most interesting part of the spectrum, had the additional effect of placing the zero-order grating image close to the S2/S3 chip gap. This is not a concern from the scientific point of view, since the X-ray forest search relies on the high-resolution, dispersed spectrum. However, the standard *Chandra* processing software (*Chandra* Interactive Analysis of Observations [CIAO]; M. Elvis et al. 2003, in preparation) failed to process the data properly as a result of this nonstandard aim point. In particular, the CIAO tool TG_RESOLVE_EVENTS, which assigns a wavelength and an order to each observed photon, failed. This problem was fixed in CIAO, Version 2.2, and the data were reprocessed to recover all of the observed photons. We used CIAO, Version 2.2, in all the data reduction and analysis.

We extracted spectra from each of the four observations separately,[4] and +1 and −1 orders were co-added. The four resulting spectra were then co-added to construct the full first-order spectrum. Errors in observed counts were appropriately propagated. The net observed count rate is 0.428 counts s^{-1} for the combined first-order spectrum, with 2×10^5 total net counts. The unbinned spectrum has 8192 wavelength channels with $\Delta\lambda = 0.0125$ Å. The FWHM of the line response function (LRF) is about 0.05 Å, increasing to larger values longward of about 50 Å. The spectral resolution is therefore $\lambda/\Delta\lambda \approx 500$ at 25 Å. The data span the wavelength range from 1 to 60 Å, but there is essentially no detectable flux longward of $\sim$40 Å. The understanding of the absolute wavelength calibration of *Chandra* spectra is continually evolving,[5] but the best current evidence is that

[4] See http://cxc.harvard.edu/ciao/documents_threads_gspec.html.
[5] See http://cxc.harvard.edu/cal/calreview.

the measured wavelengths near 25 Å are offset with respect to true wavelengths by an amount $0\ \text{Å} \leq \Delta\lambda \leq 0.025$ Å. While we could add a 0.0125 Å offset to all measured wavelengths and thereby make the calibration uncertainty symmetric about zero, we have instead chosen to keep the standard wavelength scale and to consider an observed feature "matched" to a predicted feature at wavelength λ_p if it lies between λ_p and $\lambda_p + 0.025$ Å.

3. ANALYSIS

In order to detect and measure absorption lines, we first need an accurate model of the unabsorbed continuum. The continuum properties of H1821+643 have been discussed by Fang et al. (2002b), so we do not examine them in detail here. We obtain a continuum for purposes of line detection by fitting a smooth model to the coarsely binned first-order spectrum. The model that we fit is

$$f(E) = K\left(\frac{E}{1\ \text{keV}}\right)^{-\Gamma} \exp[-N_{\rm H}\sigma(E)]\ , \qquad (1)$$

representing power-law emission absorbed by Galactic gas with hydrogen column density $N_{\rm H}$ and bound-free absorption cross section $\sigma(E)$. However, we found that a single power law did not provide an adequate fit over the entire range of the data, and we therefore carried out two independent fits in the range 0.3–0.7 keV (17.7–41.3 Å) and 0.6–1 keV (12.4–20.7 Å). We used the first fit to search for lines in the O VII and O VIII region, and the second to search for lines in the Ne IX and Ne X region. Obtaining an adequate representation of the data further requires that we treat the column density $N_{\rm H}$ as a free parameter rather than adopting the standard value of 3.9×10^{20} cm^{-2} (Lockman & Savage 1995); in effect, we use $N_{\rm H}$ as a parameter to describe departures from a power law, whether intrinsic to the quasar or caused by the Galactic interstellar medium. The fit parameters are as follows: in the 0.3–0.7 keV region, $K = 0.0030$ photons keV^{-1} cm^{-2} s^{-1}, $\Gamma = 2.28$, and $N_{\rm H} = 5.67 \times 10^{20}$ cm^{-2}; in the 0.6–1 keV region, $K = 0.0035$ photons keV^{-1} cm^{-2} s^{-1}, $\Gamma = 2.08$, and $N_{\rm H} = 3.69 \times 10^{20}$ cm^{-2}. Both of these fits have $\chi^2/\text{dof} \sim 1$, but visual inspection reveals some excess flux between 24 and 25 Å (see Fig. 2 [*top*]), which we have chosen to model as two Gaussian "emission lines" centered at 24.1516 and 24.5629 Å, with FWHM of 0.3035 and 0.120844 Å, respectively. The amplitudes of these features (i.e., the integrals under the Gaussians) are 1.795×10^{-5} and 9.601×10^{-6} photons cm^{-2} s^{-1}, respectively. The nature of these "emission lines" is unclear. We analyzed several data sets from the *Chandra* archive that had similar LETG/ACIS-S instrument setups to look for possible systematic calibration problems, but these did not show signs of excess flux at these wavelengths. We expect, therefore, that this flux originates either from the quasar itself or from the surrounding cluster. A physical characterization is not essential to our purposes here, since we only need to define a smooth continuum that fits our data.

Our final continuum model, therefore, consists of one of the two absorbed power laws described above (depending on the wavelength region), with the additional Gaussian emission lines in the 24–25 Å region, all modulated by the instrument response, which we fold in by creating an ancillary response file (ARF) generated for our observational setup. We began our search for potential X-ray forest systems by examining the residuals between the data and this smooth continuum model, looking for correlations between minima of the residual spectrum and the absorption wavelengths expected on the basis of the known O VI systems. Figure 1 shows the residual spectrum in the 21–28 Å region, in which the associated O VII and O VIII lines fall. The spectrum in the top panel has been convolved with a beta function of FWHM = 0.05 Å, which represents the LRF of the instrument at these wavelengths. This smoothing suppresses uncorrelated noise fluctuations relative to features that have the expected shape of true, unresolved absorption (or emission) lines, and it should therefore enhance the contrast of physical absorption features relative to photon noise. However, LRF convolution systematically broadens features and reduces their central depth (while preserving their equivalent width), so in the bottom panel we show the residual spectrum smoothed instead with a Savitsky-Golay (S-G) filter (see Press et al. 1992, § 14.8). This type of filter approximately preserves the sharpness and depth of features, but it is less effective at suppressing noise. The two approaches have complementary advantages, and in practice, the two residual spectra show significant features at nearly the same locations.

The strong line at $\lambda \approx 23.5$ Å is Galactic O I, and at somewhat shorter wavelengths, the Galactic O–K edge and features of the instrument response cause rapid variation of the model continuum (see Fig. 1 [*top*]). The open blue rectangle running from 22.2–23.6 Å marks the wavelength region in which these complications make reliable determination of residuals difficult. We have normalized the residuals of the two smoothed spectra so that, in each case, the range -1 to $+1$ contains 68% of the data points between 21 and 27.7 Å, excluding this problematic region. Dotted horizontal lines mark the symmetric range about zero that contains 90% (*top panel*) or 95% (*bottom panel*) of the data points in the same wavelength regions. Solid vertical line segments mark the expected positions of the 21.602 Å line of O VII (*green lines*) and the 18.969 Å line of O VIII (*red lines*) at the redshifts of the O VI systems found by TSJ and Oegerle et al. (2000): $z = 0.26659$, 0.24531, 0.22637, 0.22497, 0.21326, and 0.12137.[6] For brevity, we often refer to these redshifts simply as $z1$–$z6$, in descending order (right to left in Fig. 1). Squares below the line segments in the top panel have an area proportional to the equivalent width of the 1032 Å O VI line reported by TSJ or Oegerle et al. (2000). The wavelength calibration uncertainty $\Delta\lambda = 0.025$ Å corresponds to two channels in these histogram plots. As discussed in § 2, this uncertainty is not symmetric, and we expect a line associated with a given O VI system to appear in the predicted channel or in one of the two channels to its right (at higher λ). In velocity units, one channel is $0.0125\ \text{Å}(c/\lambda)/(1+z) \sim 125$ km s^{-1} (at $z = 0.2$, $\lambda = 25$ Å), and the wavelength calibration uncertainty is $\sim$250 km s^{-1}.

Visual inspection of either panel of Figure 1 shows that three of the deepest minima occur within the two-channel wavelength calibration uncertainty of the $z2$ and $z6$ O VII wavelengths and the $z6$ O VIII wavelength (26.901, 24.224, and 21.271 Å, respectively). Subsequent analysis (described below) shows the presence of absorption features that are significant at a $\gtrsim 2\ \sigma$ level at these wavelengths, so we

[6] Savage, Tripp, & Lu (1998) also find "associated" O VI absorption at the quasar redshift itself, but the corresponding O VII wavelength $\lambda = 28$ Å lies in the S3/S4 chip gap.

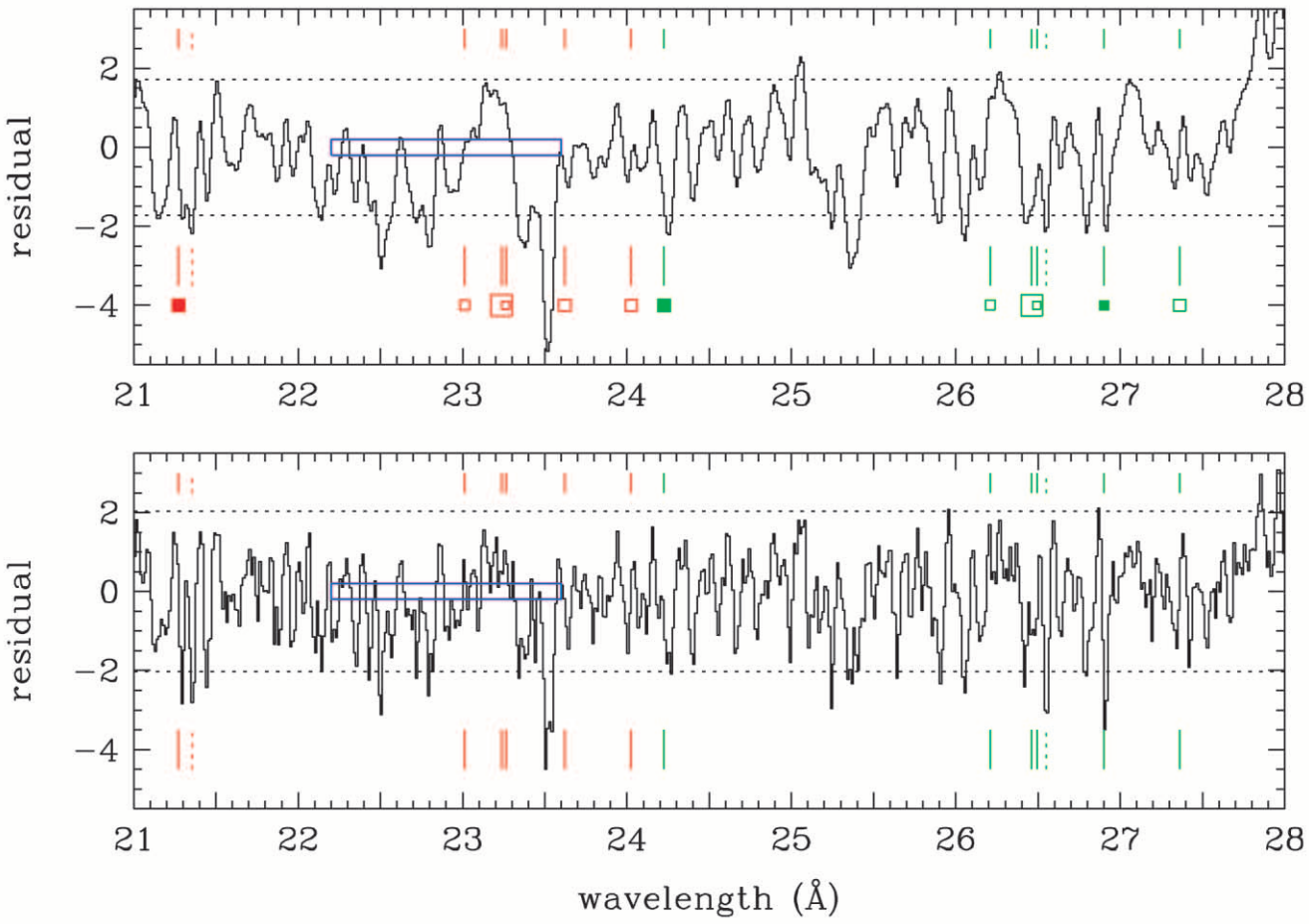

FIG. 1.—Normalized residual spectrum in the 21–28 Å region, in which O VII or O VIII absorption associated with the known O VI systems toward H1821+643 would lie. *Top*: Residual spectrum convolved with the LRF, a beta function of FWHM = 0.05 Å (individual channels in the histogram are 0.0125 Å). *Bottom*: Residual spectrum convolved instead with an S-G filter, which provides less noise suppression but better preserves the width and depth of spectral features. The open blue rectangle in each panel marks a wavelength range (22.2–23.6 Å) in which Galactic absorption and instrument response features make accurate continuum modeling difficult; the strong absorption feature at 23.5 Å is Galactic O I. In each panel, the residuals are multiplied by a normalization factor such that the range −1 to +1 contains 68% of the data values. Dotted lines mark the symmetric intervals containing 90% of the data values in the top panel and 95% in the bottom panel. Solid line segments mark the expected positions of O VII (*green lines*) and O VIII (*red lines*) absorption at the known O VI redshifts, $z1$ to $z6$ from right to left. Squares in the top panel are proportional in area to the measured O VI equivalent width. Filled squares indicate "detected" systems, for which subsequent analysis shows a line at $\gtrsim 2\,\sigma$ significance within the 0.025 Å (two-channel) wavelength calibration uncertainty of the expected position. Dotted line segments mark other features of similar strength close to expected O VII or O VIII wavelengths.

classify these systems as probable detections and mark them with filled symbols in the top panel of Figure 1. The strongest O VI system lies at $z4 = 0.22497$, and it has a weaker neighbor at $z3 = 0.22637$. There is a strong minimum in the residual spectrum just redward of the predicted O VII wavelengths, but it is not consistent with lying at either of the O VI redshifts. Since this line is comparable in significance to the O VII lines at $z2$ and $z6$, and since it lies within 1000 km s^{-1} of the strongest O VI system (and within 650 km s^{-1} of the weaker system at $z3$), we consider it a candidate for an O VII system at a nearby, but previously unknown, absorption redshift, and we mark it by dotted green vertical line segments in Figure 1. In similar fashion, we consider the feature ~1000 km s^{-1} redward of the apparent O VIII line at $z6$ to be a candidate for a new O VIII absorption line, marked by the dotted vertical red segments. There are no strong signals near the redshifts of the other O VI systems. The O VIII wavelength of the $z2$ system, $\lambda = 23.622$ Å, lies close to the Galactic O I absorption line, but we still would have been able to detect a separate line if it were present and strong. There is a strong feature at $\lambda \approx 25.35$ Å for which we have no clear identification. Its strength and breadth make it unlikely to be intervening O VII.

For quantitative assessment of features and measurement of line parameters, it is preferable to work with the unsmoothed, directly observed spectrum. Figure 2 shows the 21–28 Å region of the observed spectrum, with no extra smoothing or binning. Starting with O VII, we added to our continuum model a Gaussian absorption line at the 21.602 Å wavelength for each of the O VI redshifts $z1$–$z6$. The intrinsic FWHM of each line was fixed to be 100 km s^{-1}, similar to that of the O VI lines (TSJ); the precise value of the line width is unimportant, since the lines are unresolved if they are narrower than ~250 km s^{-1}. The normalizations of the absorption lines were thus the only new free parameters, which we determined by fitting the continuum+absorption lines model to the observed spectrum (using the continuum parameters determined previously from the coarsely binned data), folding in the effective area and the LRF. We performed this and all subsequent fits using the SHERPA software within CIAO, Version 2.2.

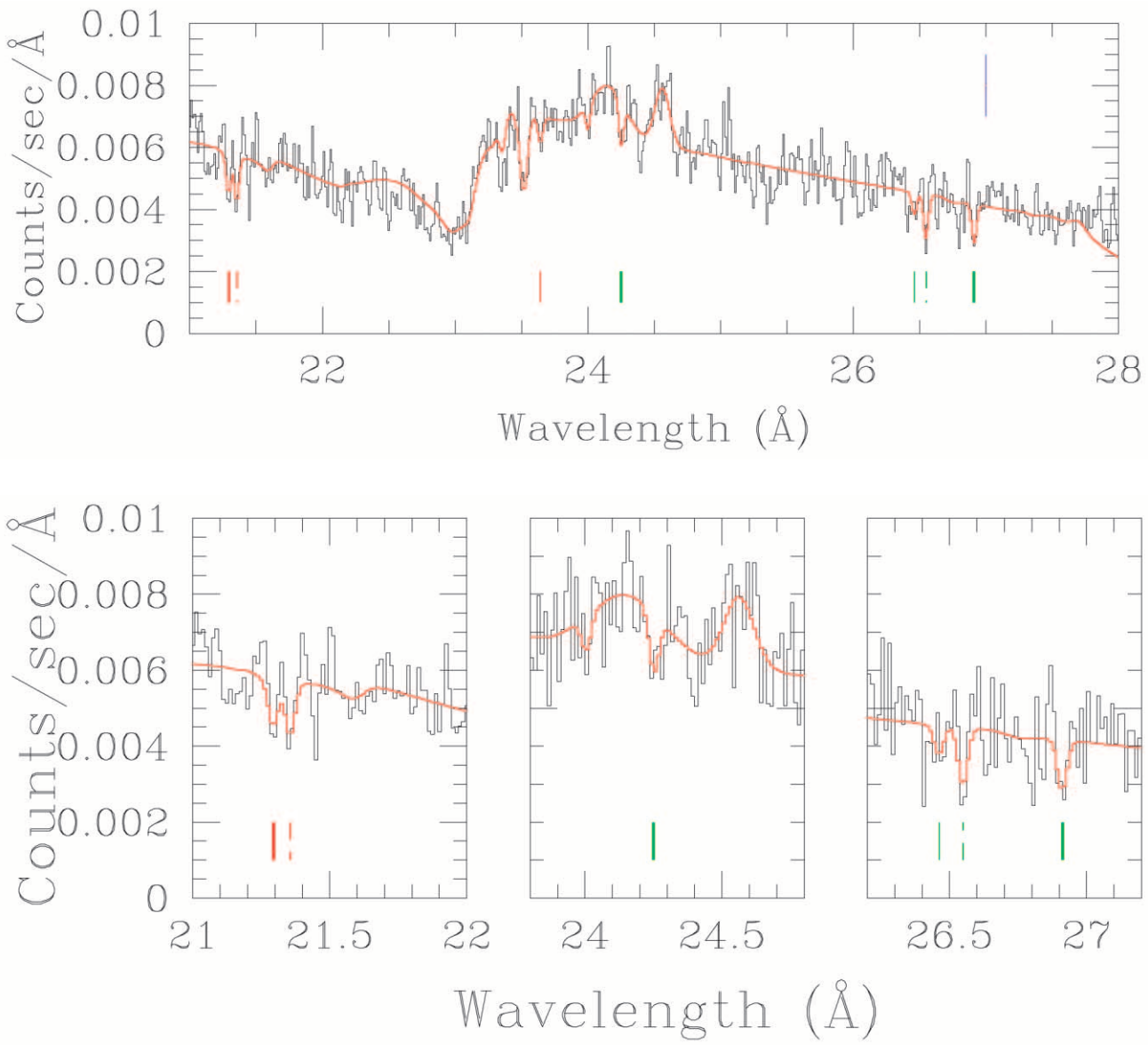

FIG. 2.—*Top*: Plot of the 21–28 Å region of the observed spectrum, with no extra binning or smoothing. The red line running through the spectrum delineates the continuum+absorption line model fit to the data. The O VII lines are marked in green, and the O VIII lines in red. The solid tick marks indicate lines at the known O VI redshifts, with thick lines indicating "detected" systems, whose significance is $\gtrsim 2\ \sigma$. The dashed tick marks indicate the candidate "new" systems, which are features of comparable strength within 1000 km s^{-1} of known O VI redshifts. The broad O I absorption line at ~23.5 Å is from the Galaxy, and the O-K edge at ~23 Å is from the instrument as well as the Galaxy. The blue bar in the top right corner of the figure represents a typical error bar. *Bottom*: Zoom on O VIII at $z6$ (*left*), O VII at $z6$ (*middle*), and O VII at $z2$ (*right*) regions showing the detected absorption lines more clearly.

This fit yielded nonzero normalizations of the absorption lines at $z2$, $z4$, and $z6$, but not at $z1$, $z3$, or $z5$, just as one might expect from visual inspection of Figure 1. To allow for the wavelength calibration uncertainty and for the possibility of small velocity offsets between O VI and O VII/O VIII absorption, we refitted the spectrum allowing the positions of the $z2$, $z4$, and $z6$ lines to vary. This fit yielded offsets of $\Delta\lambda = +0.0111$ and $+0.0274$ Å at $z2$ and $z6$, within the wavelength calibration uncertainty, while the offset at $z4$ was significantly larger. We then repeated the model fit a final time, this time fixing the $z2$ and $z6$ line positions to these best-fit values and the $z4$ line position to the original value based on the O VI redshift, with the normalizations of the $z2$, $z4$, and $z6$ systems as the free parameters. Table 1 lists the corresponding equivalent widths of the three fitted lines. The reduction in χ^2 obtained by adding each of the three lines is $\Delta\chi^2 = 4.8$, 1.27, and 2.68, with a corresponding F-test statistical significance (for one additional degree of freedom in each case) of 99.28%, 83.8%, and 95.8%, respectively. We therefore classify the $z2$ and $z6$ lines, but not the $z4$ line, as probable detections, significant at the 2–3 σ level. The 1 σ error bars quoted in Table 1 correspond to $\Delta\chi^2 = 1$ relative to the model with best-fit parameters.

Applying the same procedure at the expected wavelengths of the O VIII λ18.969 line yielded a significant detection at $z6$, a nonzero value at $z2$, and best-fit normalizations of 0 at the other O VI redshifts, just as expected from Figure 1. For the $z6$ line, there is a wavelength offset of $+0.0242$ Å, and the reduction in χ^2 is 3.51, giving an F-test significance of 98.03%. The $z2$ line reduces χ^2 by 1.08 (significance 80.4%).

TABLE 1
OBSERVED EQUIVALENT WIDTHS OF X-RAY LINES AT THE REDSHIFTS OF O VI ABSORBERS[a]

X-RAY LINES	EQUIVALENT WIDTHS (mÅ)					
	$z1$	$z2$	$z3$	$z4$	$z5$	$z6$[b]
O VII Kα.....	<6.9	13.9 ± 6.2	<6.3	7.3 ± 6.3	<6.8	9.1 ± 4.7
O VIII Kα.....	<4.7	5.2 ± 4.9	<4.9	<4.9	<4.9	9.9 ± 5.2
Ne IX Kα.....	<3.7	<3.7	<3.6	8.4 ± 3.6	<3.6	<3.4

[a] Errors are 1 σ. Upper limits (1 σ) are listed when the best-fit values of the equivalent widths are 0. All equivalent widths are in the *observed frame* and must be divided by $(1 + z)$ to obtain rest-frame values.

[b] The redshifts are $z1 = 0.26659$, $z2 = 0.24531$, $z3 = 0.22637$, $z4 = 0.22497$, $z5 = 0.21326$, and $z6 = 0.12137$. The values for $z1$–$z5$ are from TSJ (*HST*), and for $z6$ from Oegerle et al. 2000 (*FUSE*).

We also searched for absorption in the same way at the expected wavelengths of the Ne IX λ13.447 and Ne X λ12.1337 lines. This analysis yielded a line at the Ne IX wavelength at redshift $z4$, with $\Delta\chi^2 = 4.86$, and an F-test significance for one additional degree of freedom of 98.3%. The existence of detectable Ne IX for this system, which has at best weak O VII and O VIII absorption, would be remarkable, implying nonsolar abundance ratios. Nicastro et al. (2002) find evidence for supersolar Ne/O at $z \sim 0$. If the Ne IX detection here is real, the implied Ne/O ratio for this system would be higher still. There were no significant detections of Ne IX or Ne X lines for any of the other O VI systems, nor of X-ray lines from C IV, C V, N VI, or N VII.

We determined 1 σ upper limits on the strength of the O VII, O VIII, and Ne IX lines at the redshifts of the remaining O VI systems by adding lines at the expected wavelength and finding the amplitude that produced $\Delta\chi^2 = 1$ relative to the smooth continuum model. These upper limits are listed in Table 1. The O VIII limits for the $z3$, $z4$, and $z5$ systems are somewhat less secure than the others because of the complicated form of the continuum in this wavelength region. We also fitted line parameters for the two candidate "new" systems discussed earlier, one close to the $z3$–$z4$ O VII wavelength (with $z = 0.229048$) and one close to the $z6$ O VIII wavelength (with $z = 0.125847$). The derived equivalent widths and 1 σ error bars for these systems are listed in Table 2. Although these systems lie within $\sim$1000 km s^{-1} of known O VI redshifts, this condition is much less stringent than that of matching within the 0–250 km s^{-1} wavelength calibration uncertainty, making the probability of chance coincidence much higher. We therefore attribute substantially less significance to these two candidate systems, even though they are comparable in strength to the "detected" O VII and O VIII lines listed in Table 1.

TABLE 2
OBSERVED EQUIVALENT WIDTHS OF "NEW" SYSTEMS[a]

Redshifts	O VII Kα	O VIII Kα
$z = 0.229048$.....	15.1 ± 5.8	...
$z = 0.125847$.....	<5.3	11.1 ± 5.0

[a] Both new redshifts are within $\sim$1000 km s^{-1} of known O VI redshifts.

Our final model for the 21–28 Å region of the spectrum, therefore, consists of the continuum model described previously, plus O VII absorption lines at $z2$, $z4$, $z6$, and the "new" absorption redshift $z = 0.229048$, plus O VIII absorption lines at $z2$, $z6$, and the "new" redshift $z = 0.125847$. The $z4$ O VII and $z2$ O VIII features are different from 0 at the $\sim$1 σ level, while the other features are different from 0 at the $\gtrsim$2 σ level. Figure 2 shows the observed spectrum and this continuum+lines model over the full 20–28 Å region and in close-up views near the absorption redshifts. Figure 3 shows the 14–18 Å region in the same fashion. Here the model consists of the continuum with a single Ne IX absorption line at $z4$, which is different from 0 at the 2–2.5 σ level.

Since the signals we are looking for are weak, and the detection of even one X-ray forest system is of great physical import, we have been as meticulous as possible in our data reduction and analysis. In addition to the analysis reported here, we analyzed several data sets in the *Chandra* archive that have similar instrument setup to search for any hidden systematic effects, e.g., instrumental features that would produce artificially low counts in the neighborhood of our detected lines. We found no evidence for any such effects, and we are therefore confident that the features seen in Figures 1–3 are true properties of the data, not artifacts of the observational or analysis procedures.

The existence of features with $\gtrsim$2 σ significance at several wavelengths predicted a priori on the basis of O VI absorption suggests that we have indeed detected X-ray forest lines from highly ionized oxygen in these systems. However, we cannot rule out the possibility that the coincidence between observed features and known absorption redshifts is, in fact, just a coincidence. It is difficult to estimate the probability of obtaining our results "by chance" if there were no true signals in the spectrum, since the novelty of the observation was such that we could not define clear "detection" criteria in advance of seeing the data. Very roughly, we can note that three of the 12 strongest negative deviations in the 21–28 Å region of the residual spectrum lie within the 0.025 Å wavelength calibration uncertainty of a known O VI redshift. (This is true for either of the residual spectra shown in Fig. 1.) Excluding the problematic 22.2–23.6 Å region, there are about 450 channels in this spectral range and nine absorption wavelengths (six O VII and three O VIII) that could serve as possible "matches" to a given feature. The wavelength calibration uncertainty gives any of

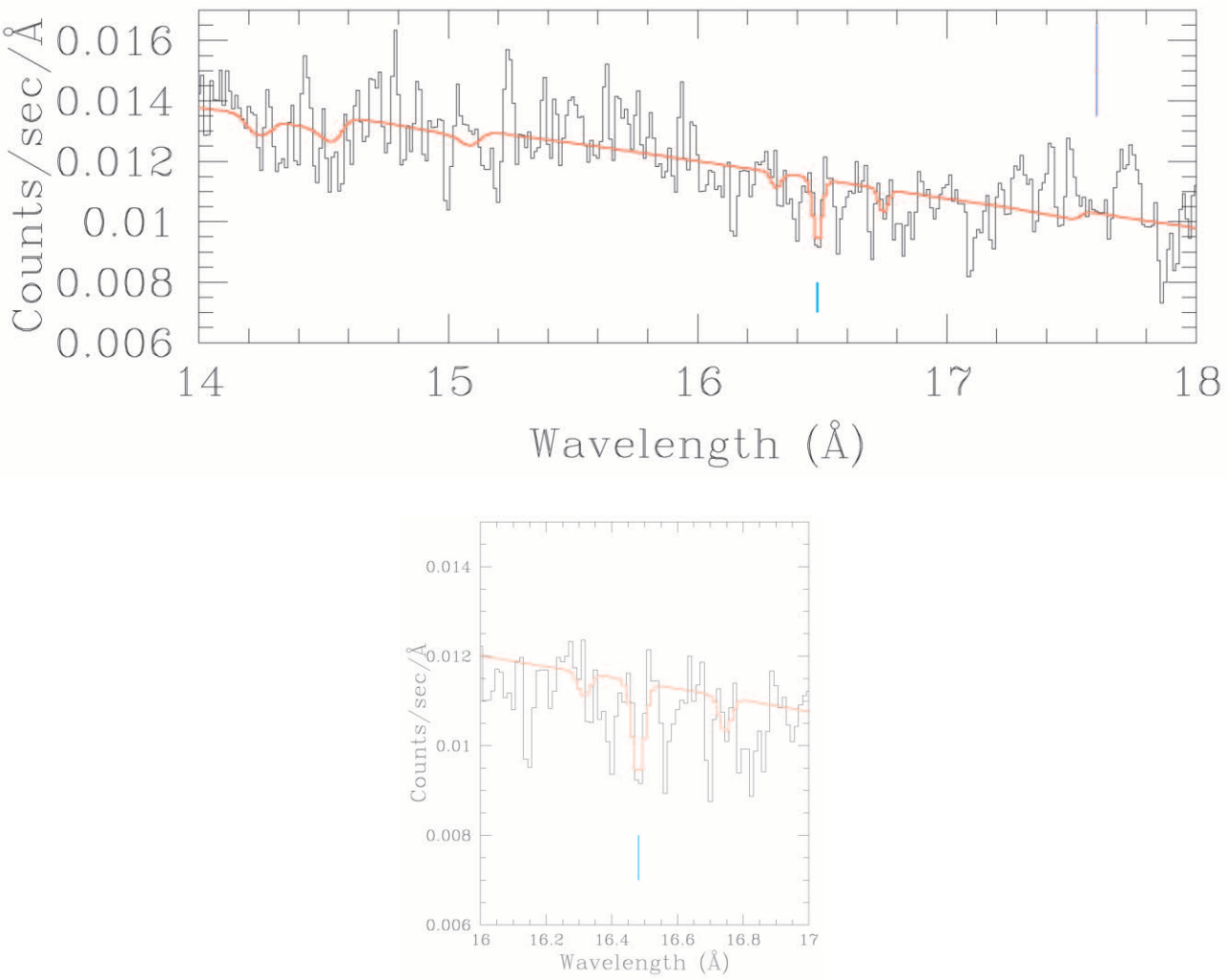

FIG. 3.—*Top*: Same as Fig. 2, but in the Ne IX region. The cyan tick mark indicates the "detected" $z4$ system. *Bottom*: Zoom on the $z4$ system.

the expected absorption wavelengths a three-channel range for a "match," so the probability that a randomly selected channel in this wavelength range matches one expected absorption system is about $9 \times 3/450 = 0.06$. The probability of getting three of the 12 strongest deviations matched with known redshifts, in the absence of a true physical correlation, is then $(0.06)^3$ multiplied by $12!/(9!3!) = 220$ (the number of ways that one can choose three distinct objects from a set of 12), or about 5%. Since this probability is not extremely small, we are cautious in interpreting our observations, considering both the possibility that we have true detections of several X-ray forest absorbers and the possibility that we have only upper limits. The only way to remove this ambiguity is to obtain a higher S/N spectrum with a longer observation.

4. IMPLICATIONS

The high density of weak O VI absorbers establishes them as an important constituent of the low-redshift universe. TSJ estimate $dN/dz \sim 48$ for O VI absorbers with rest-frame equivalent width $W_r \gtrsim 30$ mÅ, based on *HST*/STIS observations of the H1821+643 sight line. While the statistical error on this estimate is large because of the small number of systems, the discovery of an additional low-z O VI system by Oegerle et al. (2000) and of a comparable line density toward PG 0953+415 by Savage et al. (2002) supports the inference of a high cosmic incidence of O VI absorption (see Savage et al. 2002 for discussion). By constraining the absorption produced by more highly ionized oxygen species, our X-ray data provide valuable new constraints on the physical state of the O VI absorbers.

As emphasized by Hellsten et al. (1998), photoionization by the cosmic X-ray background can have an important impact on the fractional abundance of O VII and O VIII at moderate overdensities, and photoionization by the UV background can strongly influence the fractional abundance of O VI. We therefore follow the methodology of Chen et al. (2002) and calculate $f(\mathrm{O\,VII})/f(\mathrm{O\,VI})$ and $f(\mathrm{O\,VIII})/f(\mathrm{O\,VI})$ as a function of density and temperature using the publicly available code CLOUDY (Ferland 1999), incorporating photoionization by the UV background as estimated by Shull et al. (1999) and by the soft X-ray background as estimated by Miyaji et al. (1998). Figure 4 shows the fractional abundance of O V, O VI, O VII, and O VIII as a function of temperature for collisional ionization and for collisional+photoionization in gas with hydrogen number density $n_{\mathrm{H}} = 10^{-6}$, 10^{-5}, and 10^{-4} cm^{-3}. For $\Omega_b\, h_{70}^2 = 0.04$,

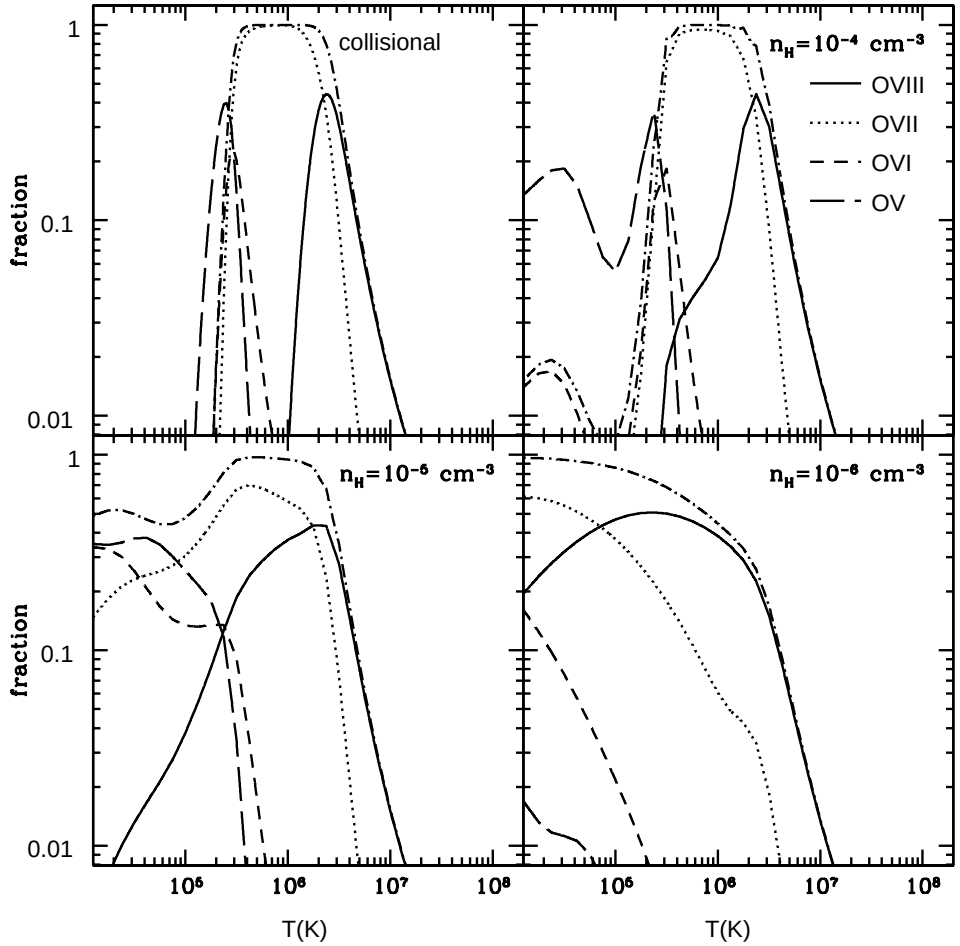

FIG. 4.—Ionization fractions of O V, O VI, O VII, and O VIII as a function of gas temperature. The top left panel shows results for pure collisional ionization. The other three panels include photoionization by the UV and X-ray background, for gas of density $n_{\rm H} = 10^{-6}$, 10^{-5}, and 10^{-4} cm^{-3}, as marked. The corresponding overdensities are $\delta_b = 6/(1+z)^3$, $60/(1+z)^3$, and $600/(1+z)^3$ for $\Omega_b\, h_{70}^2 = 0.04$. The dot-dashed line in each panel shows $f(\mathrm{O\,VI}) + f(\mathrm{O\,VII}) + f(\mathrm{O\,VIII})$, which is close to unity for temperatures 3×10^5 K $< T < 2 \times 10^6$ K and remains high at lower temperatures when $n_{\rm H} \leq 10^{-5}$ cm^{-3}. For details of the calculations, see Chen et al. (2002).

these physical densities correspond to overdensities $\delta_b \equiv \rho_b/\bar{\rho}_b = 6/(1+z)^3$, $60/(1+z)^3$, and $600/(1+z)^3$, respectively. For reference, the overdensity at the "virial boundary" of a collapsed halo is $\delta \sim 50$–150 in a flat universe with a cosmological constant and $\Omega_m \sim 0.3$, with the precise value depending on the halo profile and on the adopted definition of the virial radius (see, e.g., Navarro, Frenk & White 1997). At low temperatures and low densities, the fractional abundances are strongly influenced by photoionization, while at higher temperatures and densities, they approach the abundances expected in collisional equilibrium.

Figure 5 translates these results into contours in the $f(\mathrm{O\,VIII})/f(\mathrm{O\,VI})$ versus $f(\mathrm{O\,VII})/f(\mathrm{O\,VI})$ plane. In the left panel, curves show tracks at physical densities that correspond to $\delta_b(1+z)^3 = 1$, 10, 10^2, and 10^3, with an additional track for collisional ionization. Numbers along the tracks mark temperatures $\log T = 4.5$, 5.0, 5.5, 6.0; for $T \geq 10^{6.5}$ K, $f(\mathrm{O\,VII})/f(\mathrm{O\,VI}) > 1000$ for any overdensity. The right panel shows lines of constant temperature. For $T \lesssim 10^{5.2}$ K, the ion ratios follow a diagonal track in this plane that is essentially independent of temperature. As T increases, the tracks become more vertical, separating along the $f(\mathrm{O\,VII})/f(\mathrm{O\,VI})$ dimension. Comparing the two panels shows that $f(\mathrm{O\,VII})/f(\mathrm{O\,VI})$ is primarily a diagnostic of gas temperature, while $f(\mathrm{O\,VIII})/f(\mathrm{O\,VI})$ constrains the gas density for a given value of $f(\mathrm{O\,VII})/f(\mathrm{O\,VI})$. This behavior reflects the competing roles of photoionization and collisional ionization, with the latter being more important for higher temperatures, higher densities, and lower ionization states.

To estimate $f(\mathrm{O\,VII})/f(\mathrm{O\,VI})$ and $f(\mathrm{O\,VIII})/f(\mathrm{O\,VI})$ for the observed systems, we need to convert line equivalent widths to corresponding column densities for each ion species. The second column of Table 3 lists the O VI column densities and 1 σ error bars that TSJ and Oegerle et al. (2000) derive by fitting profiles of the 1032 Å line. Our data do not have the resolution and S/N required for profile fitting, so we instead infer O VII and O VIII column densities using the relations for optically thin lines:

$$N(\mathrm{O\,VII}) = 3.48 \times 10^{15} \mathrm{cm}^{-2} \left(\frac{W_{\rm thin}}{10\ \mathrm{m\AA}} \right), \qquad (2)$$

$$N(\mathrm{O\,VIII}) = 7.56 \times 10^{15} \mathrm{cm}^{-2} \left(\frac{W_{\rm thin}}{10\ \mathrm{m\AA}} \right), \qquad (3)$$

where $W_{\rm thin}$ is the rest-frame equivalent width (note that the observed-frame equivalent widths in Tables 1 and 2 must be

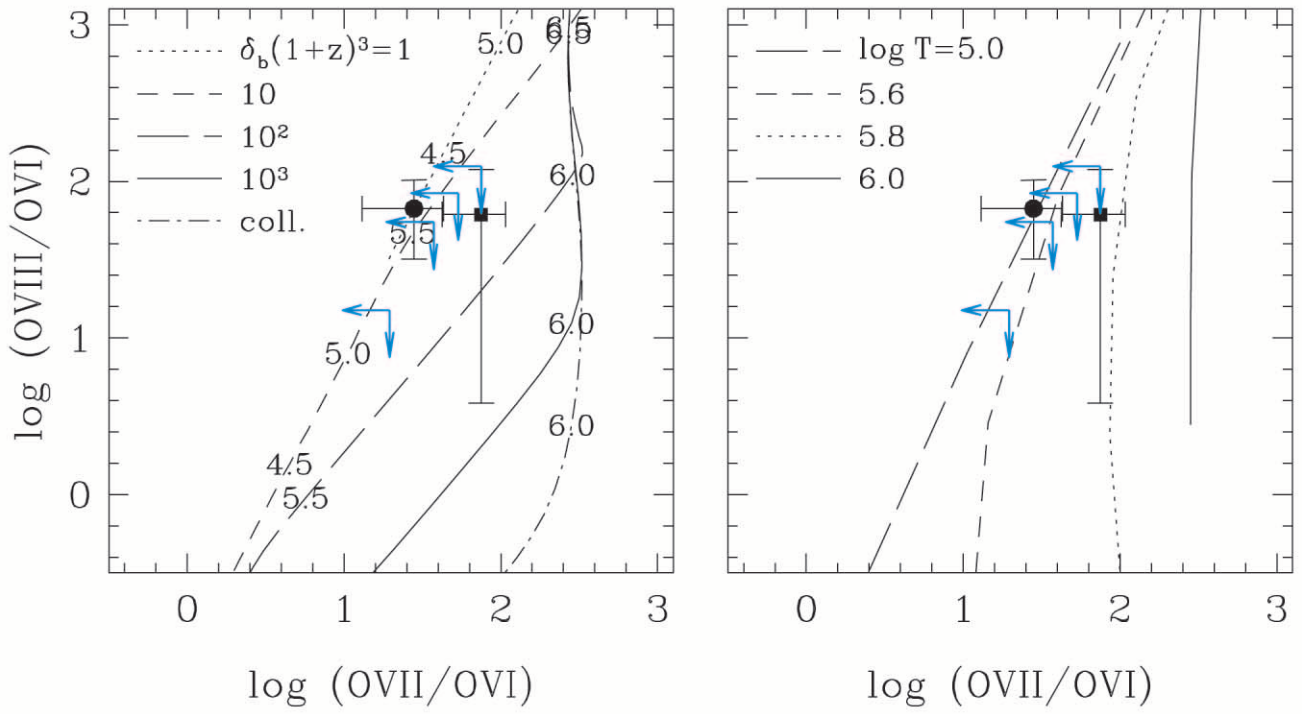

FIG. 5.—Constraints on the physical state of the known O VI absorbers. *Left*: Tracks in the $f(\mathrm{O\ VIII})/f(\mathrm{O\ VI})$ vs. $f(\mathrm{O\ VII})/f(\mathrm{O\ VI})$ plane (*curved lines*), based on the calculations illustrated in Fig. 4. Dotted, short-dashed, long-dashed, and solid lines are for gas overdensities $\delta_b(1+z)^3 = 1$, 10, 10^2, and 10^3, respectively, while the dot-dashed line represents pure collisional ionization. Numbers along these curves indicate log T in kelvins. The symbols with 1 σ error bars show the detected systems at $z2$ (*square*) and $z6$ (*circle*) at the redshifts $(1+z)^{-3} = 0.52$ and 0.71, respectively. Blue arrows indicate 1 σ upper limits for the remaining four systems at $z4$, $z1$, $z5$, and $z3$ (*bottom to top*). *Right*: Same as left panel, but with tracks of constant temperature.

divided by $1+z$ before applying these relations). Equations (2) and (3) are based on oscillator strengths of 0.70 and 0.42 for O VII Kα and O VIII Kα, respectively, taken from Verner, Verner, & Ferland (1996). The third and fourth columns of Table 3 list the corresponding column density estimates with 1 σ error bars, or 1 σ upper limits for lines with a best-fit equivalent width of 0. The $z2$ system has an inferred O VII column density of $(3.9 \pm 1.7) \times 10^{15}$ cm^{-2}, while the $z6$ system has $N(\mathrm{O\ VII}) = (2.8 \pm 1.5) \times 10^{15}$ cm^{-2} and $N(\mathrm{O\ VIII}) = (6.7 \pm 3.5) \times 10^{15}$ cm^{-2}. These are consistent with the upper limits derived by Fang et al. (2002b) from a short *Chandra* exposure. Upper limits for undetected systems are typically $\sim 1.9 \times 10^{15}$ cm^{-2} for O VII and $\sim 3 \times 10^{15}$ cm^{-2} for O VIII . The simulations of Chen et al. (2002) suggest that saturation effects for typical lines are small ($\lesssim$30%) at column densities of $N(\mathrm{O\ VII}) \leq 4 \times 10^{15}$ or $N(\mathrm{O\ VIII}) \leq 10^{16}$ cm^{-2}. We therefore expect saturation corrections to be unimportant in the case of our upper limits and limited but not entirely negligible in the case of our detections. Figure 6 shows the curve-of-growth relation for O VII and O VIII lines with b-parameters in the range 50–250 km s^{-1}, from which one can read off the column density as a function of (rest-frame) equivalent width for an assumed value of b.

TABLE 3
OXYGEN COLUMN DENSITIES IN THE INTERVENING ABSORPTION SYSTEMS[a]

Redshifts	O VI (10^{13} cm^{-2})	O VII (10^{15} cm^{-2})	O VIII (10^{15} cm^{-2})
0.26659	5.1 ± 0.8	<1.9	<2.8
0.24531	5.2 ± 0.6	3.9 ± 1.7	3.2 ± 3.0
0.22637	2.4 ± 0.5	<1.8	<3.0
0.22497	19.9 ± 1.2	2.1 ± 1.8	<3.0
0.21326	3.55 ± 0.81	<1.9	<3.0
0.12137	10.0 ± 2.0	2.8 ± 1.5	6.7 ± 3.5
0.229048*.....	...	4.3 ± 1.6	...
0.125847*.....	...	<1.6	7.5 ± 3.3

[a] The known O VI systems are in the upper part of the table, and the "new" candidate systems are at the bottom, marked by asterisks. O VI column densities are taken from TSJ and Oegerle et al. 2000 based on the stronger (1032 Å) line of the doublet. O VII and O VIII column densities are derived from the equivalent widths in Tables 1 and 2, assuming that the lines are optically thin (eqs. [2] and [3]).

In Figure 5, symbols with 1 σ error bars mark the two detected O VI systems at $z2$ and $z6$, with ion ratios based on the numbers in Table 3. Since the fractional errors in O VI column densities are far smaller than those in the O VII or O VIII column densities, we have ignored them in calculating the errors on column density ratios. For the remaining four systems, we plot arrows showing the 1 σ upper limits on $f(\mathrm{O\ VII})/f(\mathrm{O\ VI})$ and $f(\mathrm{O\ VIII})/f(\mathrm{O\ VI})$. Since the upper limits on the strength of the X-ray forest lines are roughly constant from system to system, the upper limits on the ion ratios are, to a first approximation, inversely proportional to the O VI column density. The main exception is the O VII line of the $z4$ system, for which the best-fit column density is 1 σ different from 0. The best-fit $f(\mathrm{O\ VII})/f(\mathrm{O\ VI})$ ratio of this system lies near the left-hand edge of the horizontal arrow.

At the $\sim$1 σ level, our measurements and limits have a number of interesting implications. First, there are varia-

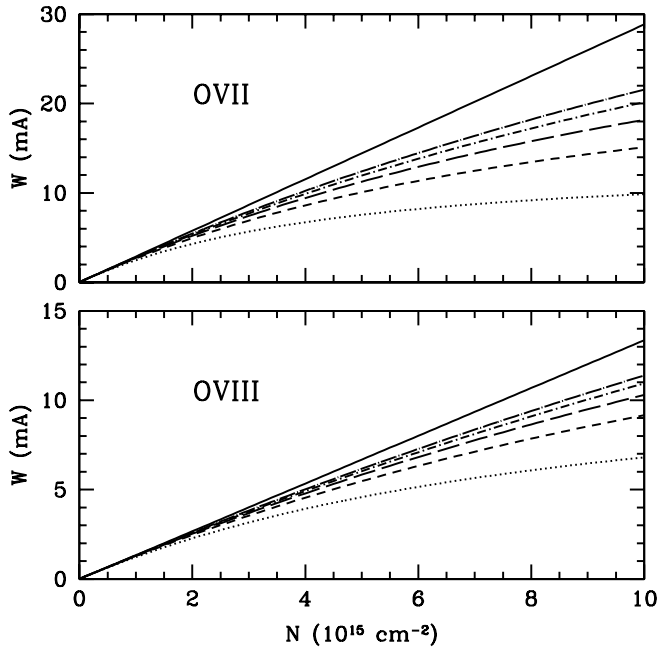

FIG. 6.—Curves of growth for O VII (*top*) and O VIII (*bottom*). Absorption line equivalent width is plotted as a function of column density for velocity width parameters $b = 50$, 100, 150, 200, and 250 km s^{-1}, from bottom to top. The top curve in both panels is for the optically thin limit.

tions in the ion ratios from system to system: the lower limit on $f(\mathrm{O\,VII})/f(\mathrm{O\,VI})$ for the $z2$ system is above the upper limit for the $z4$ and $z1$ systems, and the lower limit on $f(\mathrm{O\,VIII})/f(\mathrm{O\,VI})$ for the $z6$ system is above the upper limit for the $z4$ system. Given the sensitivity of the abundance ratios to density and temperature, it is not particularly surprising to find that they vary from system to system, but these results suggest that the diversity in physical properties will be important in understanding the contribution of O VI systems to the baryon budget. The $z2$ and $z6$ systems have a higher $N(\mathrm{O\,VI})/N(\mathrm{H\,I})$ than the other four systems (TSJ; Oegerle et al. 2000), perhaps implying higher gas temperatures that also account for the higher relative abundance of O VII and O VIII. Second, the upper limits on the undetected systems restrict their locations in the temperature-density plane; roughly speaking, the absence of detectable O VII provides an upper limit on the gas temperature, and the absence of detectable O VIII provides a lower limit on the gas density for a given temperature. For example, the $z4$ system must have $T \lesssim 10^{5.5}$ K, and if it is close to this temperature, it must have $\delta_b \gtrsim 5$. Third, the overdensities implied by the best-fit line parameters of the detected systems at $z2$ and $z6$ are significantly below the values $\delta_b \sim 100$ corresponding to virialized systems. In physical terms, the coexistence of detectable amounts of O VI, O VII, and O VIII requires that photoionization play a central role in determining the abundance ratios, which is possible only if the density is fairly low.

The last of these conclusions is the most interesting, and also the most surprising. In the case of the $z2$ absorber, the density implied by the best-fit abundance ratios is $n_{\mathrm{H}} \sim 10^{-5}$ cm^{-3}, corresponding to $\delta_b(1+z)^3 \sim 60$. If we assume that $f(\mathrm{O\,VII}) + f(\mathrm{O\,VIII}) \approx 1$, then the path length required to produce the estimated column density $N(\mathrm{O\,VII}) + N(\mathrm{O\,VIII}) = 7.1 \times 10^{15}$ cm^{-2} is $L = (3\ \mathrm{Mpc}) \times (Z/0.1\ Z_\odot)^{-1}$, where Z is the metallicity and we take solar relative abundances, $n_{\mathrm{O}}/n_{\mathrm{H}} = 7.41 \times 10^{-5}(Z/0.1\ Z_\odot)$, from Verner et al. (1996). This path is rather long for a system of $T \sim 10^{5.8}$ K, unless the metallicity is significantly above $0.1\ Z_\odot$, but the ion ratios of this system are consistent at the $1\ \sigma$ level with a density an order of magnitude higher, which would reduce the implied path length by the same factor. The $z6$ system is more of a puzzle. Taking $\delta_b(1+z)^3 \sim 10$ (higher than the best-fit value, but easily within the $1\ \sigma$ error bar), the path length implied by a similar calculation is $L \sim (24\ \mathrm{Mpc})(Z/0.1\ Z_\odot)^{-1}$, which would be long even for $Z = Z_\odot$. Typical path lengths through groups or across filaments are $\sim$0.5–2 Mpc. Even though one could in principle look along a filament and build up path length, the required alignment is improbable, and Hubble flow along the line of sight should produce a velocity width $\sim HL$ (reduced somewhat by infall velocities), while our observed lines appear to be unresolved, and the FWHM of the Oegerle et al. (2000) O VI line is $\sim$250 km s^{-1}. (The TSJ O VI line at redshift $z2$ has a smaller FWHM $\sim$ 50 km s^{-1}.)

One possibility, of course, is that the true abundance ratios of this system lie outside the range of our $1\ \sigma$ error estimates. In particular, if $f(\mathrm{O\,VIII})/f(\mathrm{O\,VI})$ is substantially lower than our estimate, then the density of the system could be much higher, and the implied path length shorter. The implied density would also be higher if the inferred O VII column density has been artificially depressed by saturation. A third possibility is that the absorber is multiphase, with the O VIII (and perhaps O VII) absorption arising in hotter gas. In this case, the ion ratios do not yield accurate constraints on the density. Higher S/N observations could rule out (or confirm) the first possibility, and good constraints on the line width from UV observations could address the second, but the last is an unavoidable source of systematic uncertainty in the interpretation of measurements such as these.

Unfortunately, our constraints at the $2\ \sigma$ level are rather weak. The O VII and O VIII fractions of the detected systems are consistent with 0 at the $\sim 2\ \sigma$ level. One can see the approximate $2\ \sigma$ upper limits for these systems in Figure 5 by adding $\log(3/2) \approx 0.18$ to the points. Similarly, one obtains approximate $2\ \sigma$ upper limits for the undetected systems by adding $\log 2 \approx 0.3$ to the $1\ \sigma$ upper limits shown in Figure 5. The conclusion that $T < 10^6$ K, with a tighter upper limit for stronger absorbers, holds robustly, but stronger physical constraints on the O VI systems at the $2\ \sigma$ level require higher S/N than our present observations afford.

What can we say about the contribution of O VI absorbers to the cosmic baryon budget? TSJ estimate this contribution based on their STIS observations of H1821+643, using the equation

$$\Omega_b(\mathrm{O\,VI}) = \frac{\mu m_{\mathrm{H}} H_0}{\rho_c c} \frac{1}{\Delta X} \left(\frac{\mathrm{O}}{\mathrm{H}}\right)^{-1} \times \langle [f(\mathrm{O\,VI})]^{-1} \rangle \sum_i N_i(\mathrm{O\,VI})\ . \quad (4)$$

Here ρ_c is the critical density, ΔX is the absorption distance interval (Bahcall & Peebles 1969) probed by the observations, and $N_i(\mathrm{O\,VI})$ is the O VI column density in system i. The factor $(\mathrm{O/H})^{-1}[f(\mathrm{O\,VI})]^{-1}$ converts the O VI column density of a system to the hydrogen column density, and the average represented by $\langle \ldots \rangle$ should be weighted by O VI column density for equation (4) to hold. In fact, $(\mathrm{O/H})^{-1}$

should be inside the $\langle \ldots \rangle$ as well, but since our observations give no additional purchase on the metallicity, we assume that it is constant from system to system. Adopting uniform values of $[\mathrm{O/H}] = -1$ and $f(\mathrm{O\,VI}) = 0.2$, TSJ find $\Omega_b(\mathrm{O\,VI}) = 0.0043\ h_{70}^{-1}$. Since $f(\mathrm{O\,VI}) = 0.2$ is close to the maximum possible O VI fraction, TSJ interpret this estimate as a lower limit on $\Omega_b(\mathrm{O\,VI})$ for $[\mathrm{O/H}] = -1$. More generally, we can express the TSJ result as

$$\Omega_b(\mathrm{O\,VI})_{\mathrm{TSJ}} = \left(0.0043\ h_{70}^{-1}\right)\left(\frac{0.1}{10^{[\mathrm{O/H}]}}\right)\left(\frac{\langle [f(\mathrm{O\,VI})]^{-1}\rangle}{5.0}\right). \quad (5)$$

Subsequent observations of three other sight lines (Richter et al. 2001; Sembach et al. 2001; Savage et al. 2002) suggest that the density of O VI absorbers toward H1821+643 may be higher than average and that the TSJ estimate should perhaps be revised downward by about a factor of 2 (Savage et al. 2002).

While small number statistics and the unknown metallicity are both significant sources of uncertainty in the $\Omega_b(\mathrm{O\,VI})$ estimates, the major uncertainty in equation (4) is the O VI ionization fraction, since $\langle [f(\mathrm{O\,VI})]^{-1}\rangle$ could quite plausibly be an order of magnitude larger than the factor of 5.0 adopted by TSJ. However, since $f(\mathrm{O\,VI}) + f(\mathrm{O\,VII}) + f(\mathrm{O\,VIII})$ should be close to unity in most systems that have detectable O VI (see Fig. 4), it is just this factor that the *Chandra* spectrum allows us to estimate:

$$\langle [f(\mathrm{O\,VI})]^{-1}\rangle \approx \frac{\sum_i N_i(\mathrm{O\,VI}) + N_i(\mathrm{O\,VII}) + N_i(\mathrm{O\,VIII})}{\sum_i N_i(\mathrm{O\,VI})}. \quad (6)$$

The sums in equation (6) weight $[f(\mathrm{O\,VI})]^{-1}$ by O VI column density, as desired for the $\Omega_b(\mathrm{O\,VI})$ estimate.

For our *estimate* of $\langle [f(\mathrm{O\,VI})]^{-1}\rangle$, we use the measured values of $N(\mathrm{O\,VII})$ and $N(\mathrm{O\,VIII})$ for the $z6$ system and of $N(\mathrm{O\,VII})$ for the $z2$ system; we use $N(\mathrm{O\,VIII}) = 0$ for the $z2$ system, and we set $N(\mathrm{O\,VI}) + N(\mathrm{O\,VII}) + N(\mathrm{O\,VIII}) = 5N(\mathrm{O\,VI})$ for the other four systems. In other words, we treat all of our 2 σ detections as real, but where we have only 1 σ measurements or upper limits, we conservatively assume the lowest O VII and O VIII column densities consistent with the physical expectation that $f(\mathrm{O\,VI}) \leq 0.2$. To obtain a 1 σ error bar on this estimate, we sum the errors of the three detected X-ray lines in quadrature, and we ignore the much smaller contribution from uncertainty in the O VI column densities. This calculation yields $\langle [f(\mathrm{O\,VI})]^{-1}\rangle = 32 \pm 9$. Combined with the TSJ result (eq. [5]), this ratio implies $\Omega_b(\mathrm{O\,VI}) = 0.028 \pm 0.008\ h_{70}^{-1}$ for $[\mathrm{O/H}] = -1$.

The statistical error bar here accounts *only* for the observational uncertainties in the $N(\mathrm{O\,VII})$ and $N(\mathrm{O\,VIII})$ measurements, not the uncertainty due to the small number of systems along the single line of sight employed in the analysis, which is probably at least as important. Furthermore, each of our detected features is consistent with 0 at the $\sim$2 σ level, and we cannot rule out the possibility that the apparent association between these features and O VI redshifts is coincidental. Nonetheless, this analysis of the *Chandra* spectrum of H1821+643 provides the first direct evidence that (1) the column density-weighted mean value of $[f(\mathrm{O\,VI})]^{-1}$ is substantially higher than the conservative value of 5.0 that TSJ and Savage et al. (2002) used to derive lower limits on $\Omega_b(\mathrm{O\,VI})$ and (2) as a result, the baryon fraction associated with O VI absorbers substantially exceeds that of any other known low-redshift baryon component, representing an appreciable fraction of the baryons predicted by BBN. The combined column density of the candidate "new" O VII and O VIII lines is comparable to that of the three lines at O VI redshifts, so these systems, if real, would represent a hotter IGM component containing a similar baryon fraction.

The estimate of $\langle [f(\mathrm{O\,VI})]^{-1}\rangle$ requires that we treat the 2 σ lines as real detections. More conservatively, we can derive an upper limit on $\langle [f(\mathrm{O\,VI})]^{-1}\rangle$ without taking a stand one way or the other on the reality of the detections. Of course, since our conservative estimate already implies $\Omega_b(\mathrm{O\,VI})$ of the same order as Ω_{BBN}, these upper limits are not very restrictive. For the 1 σ upper limit, we carry out the sum in equation (6) including $N(\mathrm{O\,VIII})$ from the $z2$ system and $N(\mathrm{O\,VII})$ from the $z4$ system, and we add to it the quadrature sum of the 1 σ errors on $N(\mathrm{O\,VII})$ and $N(\mathrm{O\,VIII})$ for all six systems, dividing the total by $\sum_i N_i(\mathrm{O\,VI})$. For the corresponding 2 σ upper limit, we simply double the error bars on each system. The result is $\langle [f(\mathrm{O\,VI})]^{-1}\rangle < 60$ at 1 σ and $\langle [f(\mathrm{O\,VI})]^{-1}\rangle < 79$ at 2 σ. In combination with the TSJ or Savage et al. (2002) numbers, even the 1 σ upper limit is consistent with $\Omega_b(\mathrm{O\,VI}) \approx \Omega_{\mathrm{BBN}}$. If we had obtained null results for all of the O VI systems, then the upper limit on $\Omega_b(\mathrm{O\,VI})$ would have come out well below Ω_{BBN}.

O VII lines with observed-frame $W \gtrsim 26$ mÅ, or O VIII lines with $W \gtrsim 20$ mÅ, would have appeared in our data unambiguously, with significance $\gtrsim 4$ σ. We can clearly rule out the existence of such systems along this line of sight. If we exclude the 22.2–23.6 Å region, then the observable path length for the O VII systems is $\Delta z = 0.2322$, and for O VIII systems, $\Delta z = 0.2232$. We therefore estimate that the number density of such systems is $dN/dz < (\Delta z)^{-1} \sim 4$ in each case. For Poisson statistics, the probability of finding no systems where three are expected is $e^{-3} \approx 0.05$, so the 95% confidence limit on the density of strong O VII and O VIII lines is $dN/dz \lesssim 12$.

In fact, even the existence of the systems that we have detected at the 2–3 σ level is rather surprising relative to theoretical expectations. For IGM metallicity $[\mathrm{O/H}] = -1$, hydrodynamic simulations predict one O VII system per unit redshift above column density $N \sim 10^{15}$ cm^{-2}, with a similar result for O VIII, and a rapid decline in the line density for higher column density thresholds. We base this statement on Figure 7 of Chen et al. (2002), but the comparisons in that paper suggest that the Hellsten et al. (1998) or Fang et al. (2002a) simulations would yield similar results for the same metallicity assumption, at least within a factor of $\sim$2. Adding scatter to the IGM metallicities increases the probability of finding strong O VII or O VIII systems, since there are more low (total) column density systems to scatter to high (oxygen) column densities than vice versa. With the metallicity scatter predicted by Cen & Ostriker (1999b), the line density predicted by Chen et al. (2002) falls to $dN/dz \sim 1$ at thresholds of $N(\mathrm{O\,VII}) \sim 2 \times 10^{15}$ cm^{-2} and $N(\mathrm{O\,VIII}) \sim 3 \times 10^{15}$ cm^{-2}. It remains surprising to find two to four systems (two if we count only those at O VI redshifts, four if we count the candidate "new" systems) with column density in excess of 4×10^{15} cm^{-2} in a path length of $\Delta z \sim 0.23$. The incidence of O VI absorption toward H1821+643 appears to be higher than average (Savage et al. 2002), and the same could be true for O VII and O VIII absorption. Nonetheless, accounting for the systems reported here within the framework of the Λ-dominated cold dark matter cosmological model (or at least the Chen

et al. [2002] simulation of it) requires that some regions of the shock-heated IGM be enriched to metallicities several times higher than [O/H] = −1, and it probably requires that the frequency of such enriched regions be higher than the Cen & Ostriker (1999b) model predicts. Confirmation of the observed systems at higher S/N, and correspondingly improved estimates of the O VII and O VIII column densities, would allow firmer assessment of the theoretical predictions for X-ray forest absorption.

5. CONCLUSIONS AND OUTLOOK

In combination with *HST* and *FUSE* observations of O VI absorption, this *Chandra* spectrum of H1821+643 provides the most direct evidence to date for the pervasive, moderate-density, shock-heated IGM predicted by leading cosmological models. The spectrum shows absorption signals with $\gtrsim 2\ \sigma$ significance at the expected wavelengths of O VII and O VIII absorption for one of the O VI systems, at the expected wavelength of O VII absorption for another, and at the expected wavelength of Ne IX absorption for a third. There are two absorption features of comparable strength within 1000 km s^{-1} of predicted O VII and O VIII absorption wavelengths, which could represent additional absorbing gas in the large-scale environment of the O VI systems. Some of the other $\sim 2\ \sigma$ features in the spectrum could correspond to X-ray forest systems without associated O VI absorption, but these features are present in roughly the number expected for Gaussian noise, so without an a priori reason to search for absorption at their observed wavelengths, we have no convincing evidence that they represent physical systems. There is a clear detection of Galactic O I absorption and a strong, broad feature at 25.35 Å for which we have no obvious identification.

The best estimates of the ratios $N(\mathrm{O\,VII})/N(\mathrm{O\,VI})$ and $N(\mathrm{O\,VIII})/N(\mathrm{O\,VI})$ for the two detected O VI systems imply that they are largely photoionized and that gas densities are significantly below those expected in virialized structures such as groups or clusters. This inference relies on the assumption that the O VI, O VII, and O VIII absorption arise in the same gas, not in different components of a multiphase system. Independent of the single-phase assumption, the measured ratios imply that the column density–weighted mean value of $[f(\mathrm{O\,VI})]^{-1}$ is substantially higher than the value of 5.0 that TSJ used to derive their lower limits on $\Omega_b(\mathrm{O\,VI})$, the baryon density associated with O VI absorbers. TSJ and Savage et al. (2002) find $\Omega_b(\mathrm{O\,VI}) \sim 0.002$–$0.004\ h_{70}^{-1}$ for [O/H] = −1 and $[f(\mathrm{O\,VI})]^{-1} = 5$, and our results imply that $\langle [f(\mathrm{O\,VI})]^{-1} \rangle = 32 \pm 9$ at 1 σ. At face value, therefore, our measurements suggest that the baryon fraction associated with O VI absorbers is substantially larger than that in stars, cold gas, or hot gas detected in X-ray emission and that the O VI absorbers trace a significant reservoir of the "missing" low-redshift baryons. The candidate O VII and O VIII systems that are not at the O VI redshifts contain a similar total amount of highly ionized oxygen. In combination with the results of hydrodynamic simulations (Hellsten et al. 1998; Fang et al. 2002b; Chen et al. 2002), the existence of even one or two X-ray forest lines at the column densities of our detected systems suggests that some regions of the shock-heated IGM have been enriched to well above $0.1\ Z_\odot$.

Unfortunately, our results also show that definitive measurements of X-ray forest absorption are extraordinarily difficult, even with the great technological advance that *Chandra*, LETG, and ACIS-S represent over previous instruments. The absorption signals for the detected O VI systems differ from 0 only at the 2–3 σ level, and since we detect some but not all of the known O VI systems, we cannot rule out the possibility that the apparent association between these features and predicted absorption redshifts is simply a coincidence. The features at other wavelengths are not strong enough to represent clear detections of new systems. The constraints on the physical properties and associated baryon fraction of the O VI absorbers are very interesting at the 1 σ level, but with 2 σ error bars we obtain only loose constraints that are not particularly surprising, although they are still more than was previously known. *XMM-Newton* has a larger effective area than *Chandra* at soft X-ray wavelengths. However, the effective area near 25 Å is nonuniform, and it is not possible to shift the aim point (as we have done here with *Chandra*) to move instrumental features away from observationally interesting wavelengths. Furthermore, published spectra obtained with the Reflection Grating Spectrometer at these wavelengths seem to achieve lower resolution than the *Chandra*/LETG, reducing the sensitivity to narrow lines. It remains to be seen, therefore, whether *XMM-Newton* will prove as powerful as *Chandra* in X-ray forest searches.

Studies of X-ray forest absorption are among the major scientific drivers for *Constellation-X*,[7] and for the still more powerful *XEUS* mission.[8] *Chandra* and *XMM-Newton* can at best give us a glimpse of what these future missions may achieve. However, the tantalizing but still ambiguous hints of X-ray forest absorption in the H1821+643 spectrum would be frustrating to live with for half a decade or more. In our view, the best step forward in the study of the X-ray forest would be further *Chandra* observations of H1821+643, which remains the best target for such an investigation because of its X-ray brightness and well-studied O VI absorption, and because the *Chandra* spectrum presented here provides 500 ks of existing data and clear objectives for a future observation. For example, an additional 1 Ms observation would reduce the noise in the coadded spectrum by $3^{1/2}$, so any true physical features that have 2 σ significance in the current spectrum would rise to a 3.5 σ significance, making their reality entirely unambiguous, regardless of whether they lie at the redshift of a known O VI system. Conversely, since we obtain 1 σ upper limits $N(\mathrm{O\,VII}) \lesssim 1.9 \times 10^{15}$ cm^{-2} and $N(\mathrm{O\,VIII}) \lesssim 3 \times 10^{15}$ cm^{-2} for systems with no absorption signal in the current spectrum, the 1 σ upper limits in undetected systems from a coadded 1.5 Ms spectrum would imply $f(\mathrm{O\,VII})/f(\mathrm{O\,VI}) < 11[N(\mathrm{O\,VI})/10^{14}\ \mathrm{cm}^{-2}]^{-1}$ and $f(\mathrm{O\,VIII})/f(\mathrm{O\,VI}) < 18[N(\mathrm{O\,VI})/10^{14}\ \mathrm{cm}^{-2}]^{-1}$, respectively. These constraints are still not extremely strong for any individual system, but null detections for all of the known O VI systems in such a spectrum would suggest that the total amount of material they contain is not enough to represent the main reservoir of the missing low-redshift baryons.

Chandra observations can also guide the design of X-ray forest studies with future missions. If the apparent detections in our current spectrum represent real systems, then *Constellation-X* is likely to find an abundance of X-ray absorption lines tracing the enriched, shock-heated IGM.

[7] See http://constellation.gsfc.nasa.gov.
[8] See http://astro.estec.esa.nl/SA-general/Projects/XEUS.

Conversely, if the features diminish as the S/N improves, then the implication is that tall trees in the X-ray forest are rare, and that even *Constellation-X* will have to search long and hard to find them.

We thank the entire *Chandra* team for a superb mission. We are grateful to Chandra X-Ray Center scientists for extensive help in the data reduction and analysis process. We thank Jordi Miralda-Escudé, Fabrizio Nicastro, and Todd Tripp for helpful discussions. This work is supported by *Chandra X-Ray Observatory* grant GO1-2118X from the Smithsonian Astrophysical Observatory. D. H. W. acknowledges the hospitality of the Institut d'Astrophysique de Paris and support from the French CNRS during the completion of this work. X. C. is supported at Ohio State by the Department of Energy under grant DE-FG03-92ER40701, and at the Insititute for Theoretical Physics, University of California at Santa Barbara by the NSF under grant PHY 99-07949.

REFERENCES

Bahcall, J. N., & Peebles, P. J. E. 1969, ApJ, 156, L7
Brinkman, A. C., et al. 1997, Proc. SPIE, 3113, 181
Burles, S., & Tytler, D. 1997, AJ, 114, 1330
———. 1998, ApJ, 507, 732
Cen, R., & Ostriker, J. P. 1999a, ApJ, 514, 1
———. 1999b, ApJ, 519, L109
Chen, X., Weinberg, D. H., Katz, N., & Davé, R. 2002, ApJ, submitted (astro-ph/0203319)
Davé, R., Hernquist, L., Katz, N., & Weinberg, D. H. 1999, ApJ, 511, 521
Davé, R., et al. 2001, ApJ, 552, 473
Fang, T., Bryan, G. L., & Canizares, C. R. 2002a, ApJ, 564, 604
Fang, T., & Canizares, C. R. 2000, ApJ, 539, 532
Fang, T., Davis, D. S., Lee, J. C., Marshall, H. L., Bryan, G. L., & Canizares, C. R. 2002b, ApJ, 565, 86
Ferland, G. J. 1999, HAZY, A Brief Introduction to CLOUDY 94, Phys. Dept. Int. Rep., Univ. Kentucky, Lexington
Fukugita, M., Hogan, C. J., & Peebles, P. J. E. 1998, ApJ, 503, 518
Hellsten, U., Gnedin, N. Y., & Miralda-Escudé, J. 1998, ApJ, 509, 56
Hernquist, L., Katz, N., Weinberg, D. H., & Miralda-Escudé, J. 1996, ApJ, 457, L51
Lockman, F. J., & Savage, B. D. 1995, ApJS, 97, 1
Miyaji, T., Ishisaki, Y., Ogasaka, Y., Ueda, Y., Freyberg, M. J., Hasinger, G., & Tanaka, Y. 1998, A&A, 334, L13
Navarro, J. F., Frenk C. S., & White, S. D. M. 1997, ApJ, 490, 493
Nicastro, F., et al. 2002, ApJ, 573, 157
Oegerle, W. R., et al. 2000, ApJ, 538, L23
Perna, R., & Loeb, A. 1998, ApJ, 503, L135
Press, W. H., Teukolsky, S. A., Vetterling, W. T., & Flannery, B. P. 1992, Numerical Recipes in Fortran (Cambridge: Cambridge Univ. Press)
Rauch, M., & Haehnelt, M. G. 1995, MNRAS, 275, L76
Rauch, M., Miralda-Escudé, J., Sargent, W. L. W., Barlow, T., Hernquist, L., Weinberg, D. H., Katz, N., Cen, R., & Ostriker, J. P. 1997, ApJ, 489, 7
Richter, P., Savage, B. D., Wakker, B. P., Sembach, K. R., & Kalberla, P. 2001, ApJ, 549, 281
Savage, B. D., Sembach, K. R., Tripp, T. M., & Richter, P. 2002, ApJ, 564, 631
Savage, B. D., Tripp, T. M., & Lu, L. 1998, AJ, 115, 436
Sembach, K. R., Howk, C., Savage, B. D., Shull, J. M., & Oegerle, W. R. 2001, ApJ, 561, 573
Shull, J. M., Roberts, D., Giroux, M. L., Penton, S. V., & Fardal, M. A. 1999, AJ, 118, 1450
Tripp, T. M., & Savage, B. D. 2000, ApJ, 542, 42
Tripp, T. M., Savage, B. D., & Jenkins, E. B. 2000, ApJ, 534, L1 (TSJ)
Verner, D. A., Verner, E. M., & Ferland, G. J. 1996, At. Data Nucl. Data Tables, 64, 1
Weinberg, D. H., Miralda-Escudé, J., Hernquist, L., & Katz, N. 1997, ApJ, 490, 564